

Southern Galactic Plane Survey Measurements of the Spatial Power Spectrum of Interstellar HI in the Inner Galaxy

John M. Dickey, N. M. McClure-Griffiths

Dept. of Astronomy, University of Minnesota

Snežana Stanimirović

Arecibo Observatory, National Astronomy and Ionosphere Center

B. M. Gaensler¹

Center for Space Research, Massachusetts Institute of Technology

A. J. Green

School of Physics, Sydney University

ABSTRACT

Using data from the Southern Galactic Plane Survey we have measured the spatial power spectrum of the interstellar neutral atomic hydrogen in the fourth Galactic quadrant. This function shows the same power law behavior that has been found for HI in the second quadrant of the Milky Way and in the Magellanic Clouds, with the same slope. When we average over velocity intervals broader than the typical small-scale velocity dispersion, we find that the slope steepens, from $\simeq -3$ to $\simeq -4$ for the warm gas, as predicted by theories of interstellar turbulence if the column density fluctuations are dominated by variations in the gas density on small spatial scales. The cool gas shows a different increase of slope, that suggests that it is in the regime of turbulence dominated by fluctuations in the velocity field. Overall, these results confirm that the small scale structure and motions in the neutral atomic medium are well described by a turbulent cascade of kinetic energy.

Subject headings: galactic structure, ISM: structure, radio lines : 21-cm line

¹Hubble Fellow

1. Introduction

The structure of the density and velocity fields in the interstellar medium (ISM) has been studied using a variety of tracers, from spectral lines in emission and absorption to pulsar scintillation and Faraday rotation. A particularly convenient tracer is the 21-cm line of HI because it is very widespread and easily detectable from both dense and diffuse clouds and from the “intercloud” or warm neutral medium. Two sorts of structure are traced with this line: deterministic and stochastic. The former are coherent features in the density and/or velocity fields that can be interpreted dynamically as evolving physical structures, like shells, bubbles, chimneys, clouds, or streams. The latter are apparently random variations in the density of the gas as a function of position and velocity, that can best be characterized statistically. The two classes of structure are related. For example, as the shells blown by stellar winds and supernova remnants expand, they ultimately lose their separate identity and blend into the background of apparently random density fluctuations. This paper is a study of the structure of the neutral atomic medium in an area of the fourth quadrant of the Galactic plane mapped in the 21-cm line as part of the Southern Galactic Plane Survey (SGPS). Preceeding papers in this series (McClure-Griffiths et al. 2000, 2001, hereafter Paper 1 and Paper 2) presented some apparently deterministic HI structures (shells and chimneys) from the survey; this paper deals with the random fluctuations.

A favorite statistical characterization of the properties of a random density or velocity distribution is the structure function (Kaplan 1966, Rickett 1976). For the ionized medium this can be measured over a huge range of scales using the propagation of pulsar signals. This analysis leads to “the big power law in the sky” (Spangler 2001), a power law that corresponds to a Kolmogorov cascade of interstellar turbulence (Cordes and Rickett 1998 and references therein). A different function for describing the structure, which is particularly easy to apply to aperture synthesis observations of the brightness of a spectral line, is the spatial power spectrum. This is the Fourier transform of the structure function or the magnitude squared of the Fourier transform of the brightness distribution (see Goldman 2000, and references therein).

Early studies of the spatial power spectrum (hereafter SPS) of Galactic HI (Crovisier and Dickey 1983; Kalberla and Stenholm 1983) revealed, quite unexpectedly, that it has a smooth, power law form with logarithmic slope -3 ± 0.2 . This result remained unexplained for many years, even after it was demonstrated by Green (1993) that the power law shows almost exactly the same slope in another direction in the outer Galaxy. More recently Stanimirović et al. (1999) have shown that even in the Small Magellanic Cloud the same power law slope is obtained. The LMC shows similar behavior (Elmegreen et al. 2001), as do Galactic molecular clouds (Zielinsky and Stützki 1999, Dickman et al. 1990, Gautier et al. 1992). In

recent years, the relationship between this power law and the Kolmogorov energy cascade is becoming more clear (Lazarian and Pogosyan 2000, and references therein, Goldman 2000). More profoundly, the structure of the ISM as measured either by the structure function or by the SPS can be interpreted as a manifestation of the fractal geometry of the medium (Elmegreen et al. 2001, Stanimirović et al. 1999, Westpfahl et al. 1999, Stützki et al. 1998).

In this paper we concentrate on testing a simple prediction of the mathematical theory of turbulence pointed out by Lazarian and Pogosyan (2000). The theory states that the slope of the power law of the observed (two dimensional) SPS should steepen when the region sampled changes from thin to thick along the line of sight. “Thick” and “thin” here depend on whether the line of sight thickness of the gas sampled by a given velocity bandwidth is more or less than the thermal width of the line divided by the velocity gradient along the line of sight due to differential Galactic rotation. In the inner Galaxy, the steep velocity gradient allows us to make the transition from thin to thick slices by averaging over progressively broader velocity widths. The result we find is in good agreement with the prediction. This gives strong support to the Kolmogorov paradigm as an explanation for the power law, and it indirectly supports the interpretation of Elmegreen et al. (2001) that the HI disk in the LMC is thin. A similar result is found for the LMC by Padoan et al. (2001) using the related spectral correlation function technique.

The observed steepening of the power law slope of the SPS with broader velocity averaging is so clear that we attempt a more profound analysis. Interstellar turbulence includes both velocity fluctuations (small scale structure in the velocity field of the gas) and density fluctuations, each with their own structure functions. Choosing one of the cases considered by Lazarian and Pogosyan (2001), we attempt to determine the power law spectral indices of the spatial power spectra of both quantities. The results suggest that the different thermal regimes (warm and cool HI) are in fundamentally different regimes of turbulence.

2. Observations

The SGPS is a combination of two surveys of the 21-cm line and continuum emission and absorption from the southern Galactic plane ($\delta < -35^\circ$, i.e. $253^\circ < l < 357^\circ$ at $b = 0^\circ$). The Australia Telescope Compact Array (ATCA) interferometer of the Australia Telescope National Facility ² is used in its mosaicing mode to make aperture synthesis images, that are combined with single dish images using the Parkes Telescope multibeam receiver (Paper 1,

²The Australia Telescope National Facility is funded by the Commonwealth of Australia for operation as a National Facility managed by the Commonwealth Scientific and Industrial Research Organisation.

Dickey et al. 1999). The latitude coverage is $|b| < 1^\circ$ for the interferometer with extension to $|b| < 10^\circ$ with the single dish only (resolution $\sim 15'$). The resulting spectral line cubes have uniform sensitivity to all angular scales down to $\sim 100''$. The combination is done using the Miriad task IMMERGE, that provides the opportunity for careful gain balance between the single dish and interferometer images, using their respective amplitudes in the overlapping portion of the uv plane. We used the continuum images (line free) to set this relative gain factor, the line data are thus not used to scale itself at any stage. Overall flux calibration is tied to the primary southern calibration source, PKS B1934-638, that is assumed to have flux density of 14.95 Jy at 1380 MHz.

The best studied portion of the SGPS so far is our test region, which covers $326^\circ < l < 333^\circ$ and $0^\circ < b < +3^\circ$. Observations of this area were done before the main survey, to evaluate the data quality and reduction strategy. Our basic spectral line cube of this region has spectral channel spacing 0.824 km s^{-1} , pixel size $40''$, and clean beam size (FWHM) $118'' \times 125''$. This gives gain $G = 41.2 \text{ K/Jy}$, where G is defined by

$$G = \frac{2k}{\lambda^2} \times \Omega_B$$

where k is Boltzmann's constant, λ the wavelength, and Ω_B is the solid angle of the synthesized beam, that is 1.3×10^{-3} degrees 2 or 10.3 pixels in the map plane. The rms noise is 1.7 K in the spectral line channels, and the dynamic range is about 250:1 in the continuum. The area was covered as a mosaic of 190 pointings with the interferometer, of which each one was observed 40 times with “snapshots” of 30 s integration time each. The mosaic was processed with the Miriad program MOSMEM (Sault et al. 1996), that deconvolves the effects of missing uv spacings, and partially recovers the short spacing information that the interferometer misses.

For figure 1 see the jpeg image associated with this paper.

Fig. 1.— HI emission in the SGPS test region. The upper panel shows the integral in velocity over the 21-cm spectrum, at each pixel in the area. The grey bar at the top gives the scale, in units of 10^{20} cm^{-2} ($1 \times 10^{20} = 54.85 \text{ K km s}^{-1}$). Contours are drawn at 50, 100, 150, and $200 \times 10^{20} \text{ cm}^{-2}$. The light spots appear at the positions of continuum sources that show strong absorption; they appear negative because the continuum has been subtracted from the cube. The lower panel shows the longitude-velocity diagram of the HI emission at $b=+0.022$. The stripes near longitude 331.5° show the effect of absorption toward some faint continuum features, but generally this latitude has no strong continuum sources, so the l-v diagram is mostly absorption-free. Contours are drawn at 5, 30, 55, 80, and 105 K in brightness temperature.

Figure 1 shows the HI emission after continuum subtraction. The upper portion shows the velocity integral of the emission spectra in each pixel (zero moment map), and the lower portion shows the emission brightness vs. longitude and velocity along a line near latitude 0° for which there are no bright continuum sources. Individual channel maps of the 21-cm emission of this region are shown in Paper 2. The large scale Galactic structures that cross this longitude range are the Norma Arm, the Scutum-Crux Arm, and the Sagittarius-Carina Arm. Following the discussion of Paper 2 (Figure 4), the Norma Arm is near the tangent point, at galactocentric radius about 4.5 kpc and radial velocity -100 dropping to -60 km s^{-1} (LSR). We see this arm tangent to the line of sight, stretching from about 6 to 11 kpc distance. The Scutum-Crux arm is at about 3.5 kpc distance, with radial velocity -50 to -60 km s^{-1} . The Sagittarius-Carina Arm blends with the local gas at about -10 to -20 km s^{-1} . The solar circle on the far side is at about 15 kpc distance. At that distance the z-height of the top of our field ($b \simeq +3^\circ$) is about 800 pc, so the scale height of the HI layer (nominally 150 pc) comes up only to about 0.6. At the Scutum-Crux arm distance the top of our field is only at 180 pc, so at -50 km s^{-1} we see a decrease in HI brightness with b by about a factor of two to three over our latitude range.

This large scale structure of the inner Galaxy is not strikingly apparent on the longitude-velocity diagram of Figure 1 for three reasons. The first is that, unlike CO and other tracers of gas in high density environments, the HI 21-cm emission coefficient depends only on the density and not on the temperature. Atomic hydrogen is quite widespread, with a filling factor of 25% or more in the inner Galaxy, so the inter-arm regions are not empty of HI. But in the high density environment of the spiral arms, most of the HI is converted to H_2 , so the 21-cm emissivity no longer traces the total density of hydrogen (Allen 2001). Large scale Galactic structure typically causes only moderate variations in the HI emissivity, that are reflected in variations of a factor of two or three in the spectrum of brightness temperature vs. velocity. The second problem is that large scale departures from circular rotation can cause as much structure in the emission spectra as density variations (Burton 1971). Thus the details of the l - v diagram depend as much on the velocity structure of the spiral pattern as they do on the local emissivity variations. Finally, the third complicating factor is self-absorption in the 21-cm line. The optical depth of the HI is on the order of one over roughly 30% of the inner Galaxy velocity range (here negative velocities). A full analysis of this effect is beyond the scope of this paper, we will present a more extensive discussion of HI absorption and HI self-absorption in a forthcoming paper.

3. Analysis

To study the SPS of the emission, we want to look where there is emission only, to avoid confusion between emission and absorption. We concentrate on two sample regions where there are no bright continuum sources, each 128 pixels square ($85.3' \times 85.3'$); region 1 extends from $(l,b) = (327.32, +1.82)$ to $(328.74, +3.23)$, region 2 extends from $(329.29, -0.01)$ to $(330.70, +1.40)$. The first is at a latitude high enough that even the diffuse continuum is faint, the latter is near $b=0^\circ$, so it has the longest lines of sight across the outer galaxy. These areas are indicated on Figure 2, that shows the continuum emission from the test region. The extended sources are mostly identified as HII regions or supernova remnants, as discussed in paper 2. Here we avoid them and their effects on the ISM. Figure 2 shows representative spectra (taken from the center of each area), with at the bottom of each an indication of the radial velocity vs. distance r along the line of sight predicted by cylindrical rotation with the rotation curve of Fich et al. (1989). The **slope** of this curve is the velocity gradient, a critical quantity for determining the line of sight depth of a given velocity interval, and thus the expected profile shape (Burton 1989). Along most of the line of sight in the inner Galaxy the velocity gradient has value $\frac{dv}{dr} = \pm 20 \frac{\text{km s}^{-1}}{\text{kpc}}$, except near the subcentral point where it necessarily goes through zero.

For each region, we apodize by multiplying each plane of the cube by a window function that is unity everywhere except near the edges of the region where it drops smoothly to zero with a Gaussian profile (Stanimirović 1999). This reduces the “edge effects” in the transform plane caused by discontinuities at the edge of the image when it is replicated in both dimensions (e.g. Brault and White 1971). Then we Fourier transform, and compute the **magnitude squared** of the Fourier components.

The transforms were done using the Miriad task FFT, that does the normalization by $\frac{1}{N}$ in the inverse transform, so values on the transform plane are typically a factor of $\sqrt{128}$ higher than on the sky plane. There are still “diffraction spikes” through the center of the transform image (pixel 65,65 is the center or “zero spacing” in the uv plane) due to the narrow width of the edge taper in the apodizing function, so we blank row 65 and column 65. Then we segment the uv plane into annuli with radii increasing logarithmically, and for each annulus we compute the mean and rms of the values of the transform magnitude squared for all pixels whose centers lie in the annulus. The results are shown in Figures 3 through 6.

Figure 3 shows the spatial power spectra of the HI emission in region 1. Each set of points connected by line segments corresponds to a single velocity channel (0.824 km s^{-1}). We plot only every 24th channel, so the lines on Figure 3 correspond to velocity channels spaced by 20 km s^{-1} from -140 to $+100 \text{ km s}^{-1}$. These include several baseline channels on

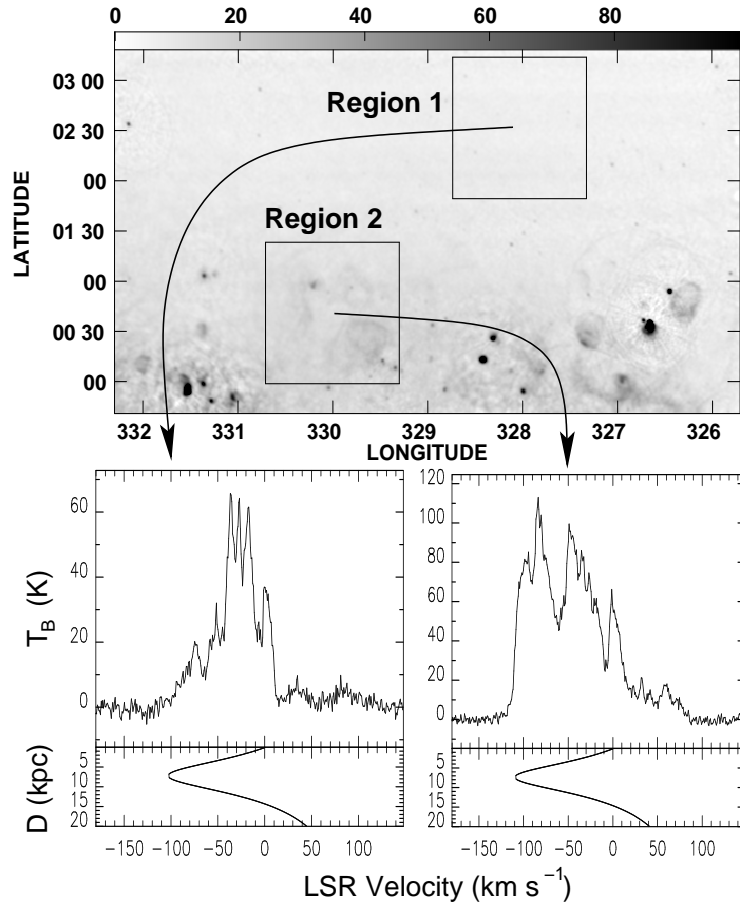


Fig. 2.— Continuum image of the SGPS test field, with the two smaller, mostly continuum-free regions indicated. The grey scale is in K of brightness temperature. The H I spectra below are taken through the central pixel (65,65) of each region. The scale below each spectrum shows the kinematic distance using the rotation curve of Fich et al. (1989).

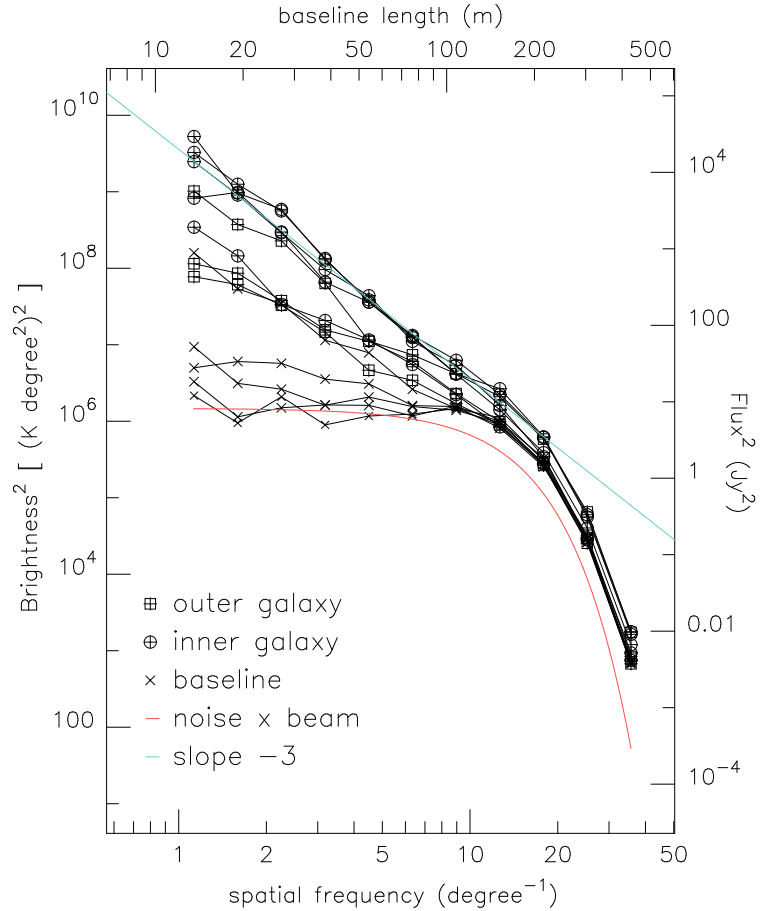


Fig. 3.— The spatial power spectrum of the HI emission in Region 1. The bottom axis scales the spatial frequency, increasing to the right (smallest angular scales). The left axis shows the magnitude squared of the Fourier Transform components of the HI distribution. The segmented lines with symbols show the data for different velocity channels, separated by 20 km s^{-1} , from -140 to $+100 \text{ km s}^{-1}$ LSR. Negative velocities (from the inner Galaxy) and positive velocities (from the outer galaxy on the far side) are distinguished by squares and circles respectively. Velocities with little or no emission (“baseline”) are marked with \times symbols. The lower curve (red in the electronic edition) shows the prediction for white noise smoothed with the synthesized beam. The straight line (blue in the electronic edition) shows a power law with index -3.

each side of the emission, five channels that sample primarily the inner Galaxy (at negative velocities), and four that sample the outer galaxy (positive velocities), indicated by different symbols on Figure 3.

Figure 3 has different units on its different axes. The bottom axis is the spatial frequency, that has units of inverse angle (here degrees^{-1}). This shows the radius on the uv plane of the middle of each annular bin. Corresponding to a given spatial frequency (number of cycles per degree) is a baseline length of the interferometer; these lengths are shown on the top scale. The original image has units of brightness temperature (K), so its transform has units of brightness temperature per pixel area, or K degree^2 . Since the images are 128 x 128 pixels at $40''$, the pixel size on the conjugate (uv) plane is $0.703 \text{ degrees}^{-1}$ and the pixel area is $0.494 \text{ degrees}^{-2}$. Finally we scale the magnitude squared of the transform components by the pixel size squared, i.e. by dividing by $(0.703 \text{ deg}^{-1})^4$ to get units of $\text{K}^2 \text{ degree}^4$. These units are indicated on the left hand scale of Figure 3.

We can alternatively convert the original image to units of Jy per beam by dividing by 41 K/Jy (the gain of the synthesized beam, G , defined above). Dividing the image in units of Jy per beam by the beam area in pixels gives units of Jy per pixel. Then the units on the transform plane are simply Jy. The corresponding squared magnitudes have units Jy^2 , as indicated on the right hand scale of Figure 3.

On Figures 3 and 4 the baseline channels show flat spectra, consistent with radiometer noise that is spatially “white”, up to the inverse of the synthesized beam size ($\simeq 120''\text{FWHM}$). The prediction for a Gaussian with $\text{FWHM} = \frac{2}{120''}$ and amplitude equal to the square of the two sigma noise level is indicated on Figures 3 and 4. Channels for which the region is filled with emission show the familiar power law SPS, with spectral index very close to -3 out to the resolution limit. Figure 4 uses only the ATCA data for region 2, while Figure 3 uses the combined Parkes plus ATCA images for region 1. The interferometer data alone show a cutoff at large angular sizes (the last column of points on the left side of Figure 4) that can only be measured with the single dish telescope. The smoothness of the spatial power spectra down to this smallest spatial frequency in Figure 3 demonstrates the quality of the calibration between the interferometer and single dish data. A few channels on Figures 3 and 4 show power law slopes flatter than -3, for example $v=+80 \text{ km s}^{-1}$ in region 1 shows slope of -1.5. Investigation of the images shows that the emission at this velocity is concentrated in a very small clump that is presumably at great distance in the outer galaxy (its nominal kinematic distance is 37 kpc). Since this emission covers an area much smaller than the area of region 1, the spatial power spectrum is dominated by the **boundaries** of the cloud, rather than its internal structure. This inevitably flattens the slope of the spectrum, since the lower spatial frequencies cannot be as strong for a small cloud as for emission that

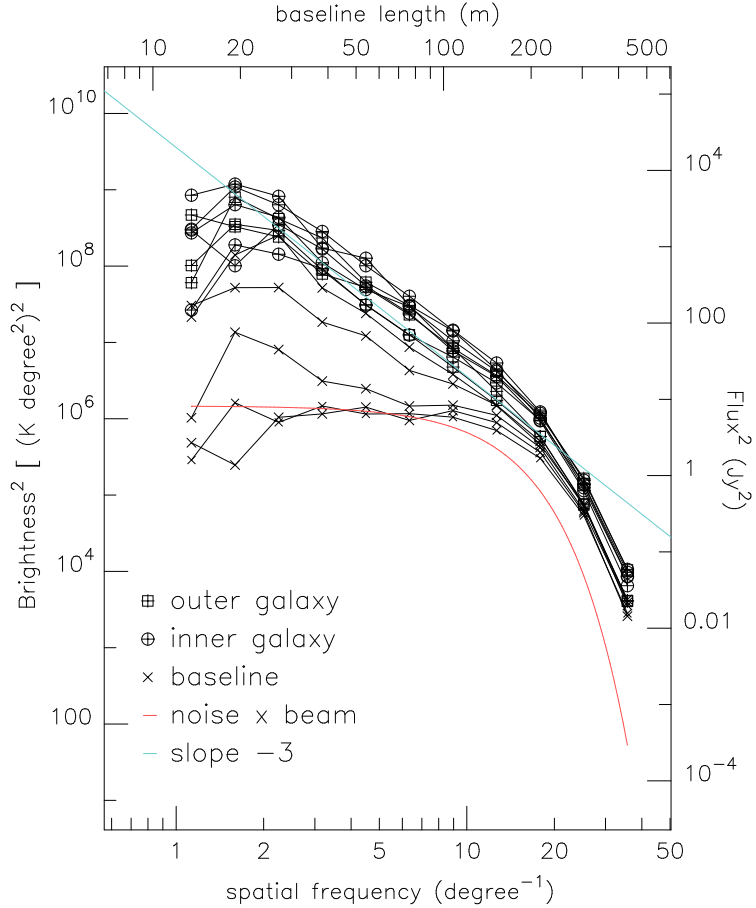


Fig. 4.— The spatial power spectrum of the HI emission in Region 2, with axes similar to those on Figure 3. This case uses the interferometer data alone, without combining with the single dish images, hence the turnover at low spatial frequencies (angles larger than about $20'$ are not well sampled by the interferometer). The straight line (blue on the electronic edition) is the same as on Figure 3, that shows that the HI emission is generally stronger at the lower latitudes, particularly at high negative velocities (near the subcentral point) and at positive velocities in the outer galaxy on the far side of the solar circle. This is an effect of the lower latitude of this region.

fills the region. In the limit of a very small cloud, barely resolved by the synthesized beam, the SPS would be flat, similar to the noise in the baseline channels on Figures 3 and 4. The different slope in this case is not evidence for different statistics of the **internal structure** of the HI cloud, that could only be measured in this way over much smaller areas entirely within the cloud’s boundaries.

Figure 5 shows velocity spectra of the amplitude squared of the Fourier components. Each panel shows the average over one of the annuli on the uv plane, starting with radius 1.2 degree^{-1} and going to 37 degree^{-1} in steps of 0.15 in the \log_{10} of the radius (i.e. factors of $\sqrt{2}$ in spatial frequency, as on Figures 3 and 4). The lowest spatial frequencies show broad, very smooth spectra, whose most significant feature is a bump at high positive velocities ($\sim +80 \text{ km s}^{-1}$) on Figure 3. This corresponds to the small cloud mentioned above. At higher spatial frequencies the spectra show more structure in velocity, but they are still smoother than any single-pixel emission spectrum from the region.

3.1. Velocity Averaging

The results presented in Figs. 3 and 4 show that the HI spatial power spectrum for both regions 1 and 2 can be fitted with a power law, over a range of angular scales from 3 arcmin to 1 degree (corresponding to length scales of 6 to 130 pc at the tangent point distance of 7.4 kpc). As region 1 is located at $b \approx 2$ degrees ($z \simeq 250$ pc at the tangent point) and does not contain significant continuum emission, the effects of absorption and HI self-absorption are not severe, and the 21-cm line intensity is generally directly proportional to the HI column density. We can therefore test predictions of the turbulence theory described in Lazarian & Pogosyan (2000, hereafter LP) on this region. This theory provides a way to relate the observed 2-D SPS of the HI brightness to the underlying 3-D statistics of both the density and the velocity distributions.

The simplest theoretical situation is the case of density fluctuations alone, with no small scale structure in the velocity field. In this case, a narrow section through the medium should show a SPS slope that differs from that of a deep sample. In the asymptotic limit of thin and thick slices described by LP (section 3), and assuming steep spectra (slope n less than -1) the difference in slope is just one unit, i.e.

$$P(\mathbf{k}) \propto \{ |k|^{n+1} \quad \text{thin} |k|^n \quad \text{thick}$$

where P is the observed SPS and k is the spatial frequency.

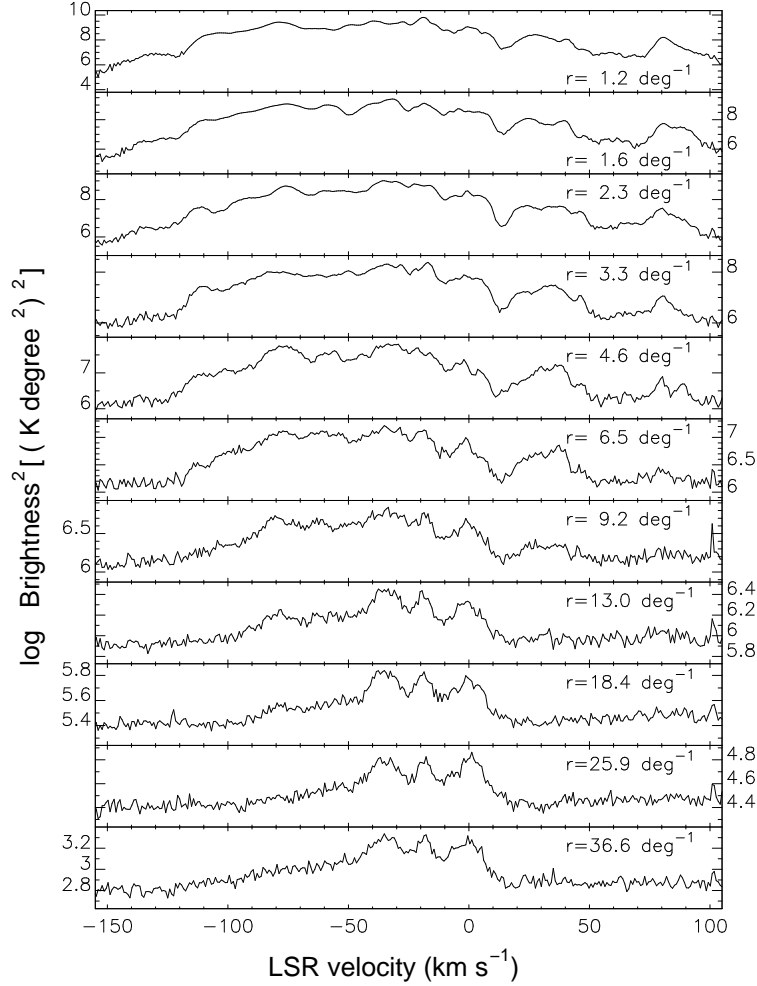


Fig. 5.— Velocity profiles of the SPS amplitude, at various uv radii. Each panel corresponds to a different column of points on Figure 3, the top panel corresponding to the leftmost column, the bottom to the rightmost column. Whereas on Figure 3 only a few velocity channels are shown, here the entire velocity range is displayed. Note that the vertical scale changes drastically from the top profile to the bottom, as indicated by the values on the scales, which alternate from side to side. For this reason the noise is much more noticeable on the lower profiles compared with the upper ones.

We can use velocity smoothing to effectively change the width of the slice, since the velocity gradient translates velocity width to line of sight depth as described above. To search for a change of slope, we average the line data over broad velocity widths in the cube for Region 1, and then recompute the SPS following the same method described above. The results are shown on Figures 6 - 8. Figure 6 is similar to figures 3 and 4, but with the spectral line data averaged over 24 channels before the Fourier transform (bandwidth 20 km s⁻¹). Based on the velocity gradient of 20 km s⁻¹ kpc⁻¹, averaging over this velocity width increases the line of sight depth of the samples from ~ 0.4 to 1 kpc. The SPS does indeed steepen, as predicted, from ~ -3.1 to ~ -4.0 in the logarithmic slope. This range includes the prediction of the simple Kolmogorov theory, $n = -\frac{11}{3}$.

We study this transition from thin to thick sections through the gas, by averaging over progressively broader bandwidths from a single 0.8 km s⁻¹ velocity channel, to three (2.5 km s⁻¹), six (4.9 km s⁻¹) and so on up to the 24 channel averages shown on Figure 6. We then fit straight lines to the spatial power spectra over the interval from 2 to 8 deg⁻¹ for each new velocity average. Results are shown on Figure 7 for representative velocity channels spaced by 30 km s⁻¹. Here we include three channels from the inner Galaxy (at -20, -50, and -80 km s⁻¹), two from the outer galaxy (+40 and +80 km s⁻¹), and one baseline channel that is mostly noise (-140 km s⁻¹). They all show some steepening, although the baseline channel fluctuates between slope 0 and slope -1.5. At velocity +70 the slope steepens from -0.5 to -2, but this is probably simply due to the small covering factor of this very distant gas, so that the broader velocity averaging includes many separate, unrelated structures in such a way as to increase the covering factor of the HI. The inner Galaxy channels are the most consistent and they best match the prediction of the turbulence model. Each one steepens smoothly (from slope -2.5 to -3.6 at -50 km s⁻¹, from -3.3 to -4.1 at -20 km s⁻¹, and -3.1 to -3.6 at -80 km s⁻¹). The last, -80 km s⁻¹, seems to flatten at the broadest bandwidths, that may be due to the velocity gradient's sharp drop to zero at the terminal velocity (~ -100 km s⁻¹ at this longitude).

Averaging more than about 20 km s⁻¹ does not significantly steepen the slope. This is shown on the upper panel of Figure 8, that plots **all** data for the inner Galaxy for a broad range of averaging widths (to 55 km s⁻¹). To make Figure 8 we compute the slope for every modified velocity channel, and then find the mean and standard deviation of the slopes. The error bars indicate $\pm \frac{\sigma}{\sqrt{s}}$ around the mean of the slopes, for the sample (size s) of all modified velocity channels with centers in the range -15 km s⁻¹ to -80 km s⁻¹.

Including the turbulence-induced fluctuations of the **velocity field** of the gas as well as density fluctuations changes the meaning of the slope. Following LP (section 4.2) we find that the power law slope of the SPS for the thin and thick slices becomes $(-3 - \frac{m}{2})$

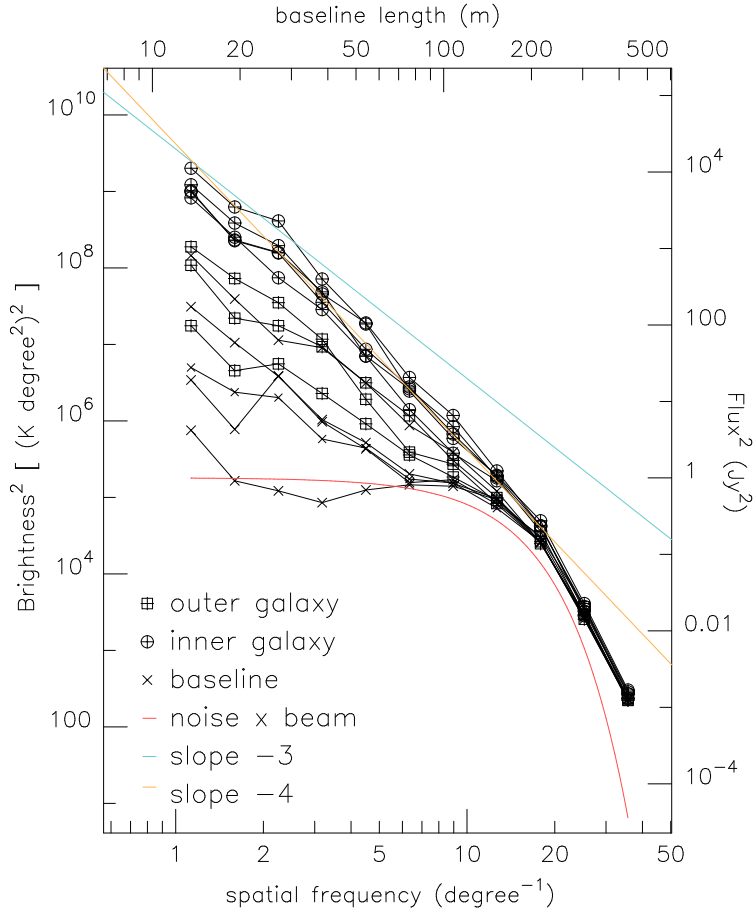


Fig. 6.— The SPS of the **velocity averaged** HI emission of region 1. This is similar to Figure 3, except that instead of analysing single-channel data separated by 20 km s^{-1} , we first average over 20 km s^{-1} velocity widths (24 channels) and then Fourier transform. The line with slope -3 (blue on the electronic edition) is the same as that on Figure 3. The steeper line (gold on the electronic edition) has slope -4. For the inner galaxy velocities, where the region is mostly covered with HI emission, the slope has changed from -3 to -4 due to the velocity averaging.

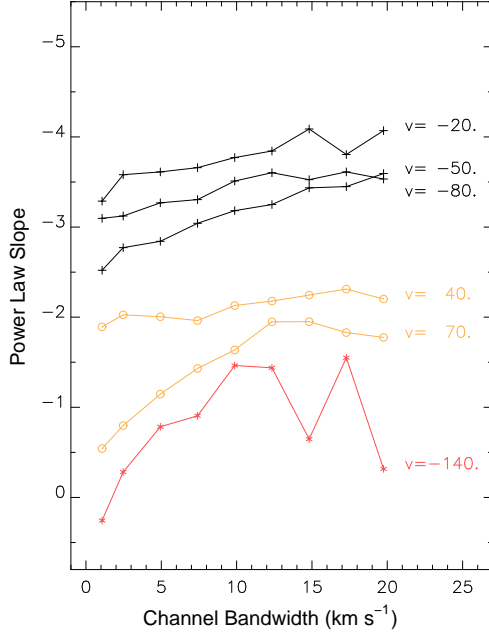


Fig. 7.— Slopes of the spatial power spectra for various velocity averaging. Each point represents a least squares fit to the logarithmic slope of the spatial power spectra (as shown on Figures 3, 4, and 6) for specific velocity channels. The cube is first averaged in velocity over progressively broader bandwidths (scaled on the bottom), thus each successive point from left to right represents an average, of one, three, six, etc. up to 24 velocity channels (20 km s^{-1} width). The three upper curves, marked with crosses (black in the electronic version) are for the inner Galaxy, centered at velocities of -20 , -50 , and -80 km s^{-1} . The bottom curve (red in the electronic edition) is mostly noise, it is a baseline channel centered at -140 km s^{-1} well beyond the terminal velocity. The middle curves, marked with circles (gold in the electronic edition), are at positive velocities that cover distant gas, well beyond the solar circle on the far side of the galaxy in the lower halo, which does not fill the field (above the noise). Typical error bars (representing both noise and the dispersion of the ensemble as measured from independent velocity channels) are ± 0.25 on the upper curves.

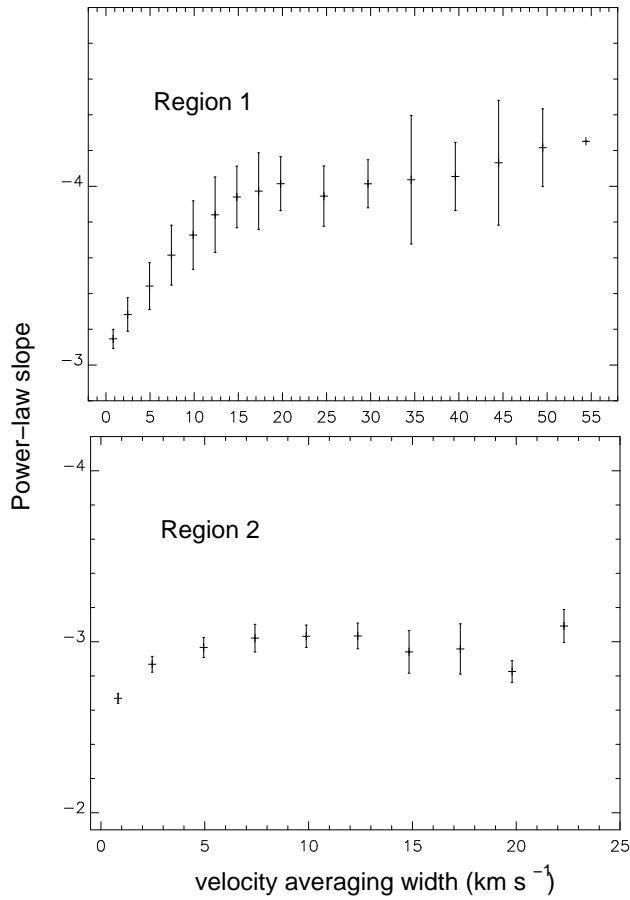


Fig. 8.— Power law slope vs. velocity averaging width. In this case we consider **all** channels with center velocity in the range -15 km s^{-1} to -80 km s^{-1} for each averaging width, and compute the mean and standard deviation of the slopes of the power spectra in each case. Results for both regions are shown. Region 2 is at such low latitude that self-absorption in the hydrogen is significant; this may mostly cancel the velocity averaging effect in the power law slope.

in the thick case and $(-3 + \frac{m}{2})$ in the thin case, where m is the power law index of the velocity structure function. The Kolmogorov case has $m = \frac{2}{3}$, that would give -2.67 and -3.33 respectively for the slopes in the thin and thick cases. If we try to force the data from region 1 to match the prediction for the velocity dominated regime, we find a steeper velocity spectral index ($m = 0.9$) but **not centered on -3**. This suggests that the velocity term is not strong enough to dominate the density term in the calculation of the SPS slope for region 1, so there we can measure n but not m .

Region 2, at much lower latitudes, shows very different behavior. The center of the region is at $b = +0^{\circ}7$, that translates to $z = 90$ pc at the tangent point. This is less than the scale height of **cool HI** (roughly 120 pc), so the line of sight is rich in cool gas, as shown by the many deep absorption lines toward continuum sources in this area. This effects the LP analysis of the SPS in two ways. First, self-absorption in the HI causes the brightness temperature to saturate, so that it no longer traces the column density of the gas. Second, the intrinsic linewidth of the emission changes from about 16 km s^{-1} to about 1.6 km s^{-1} , since the thermal velocity decreases with the temperature, that is about 6000 K in the warm HI but typically 60 K or less in the cool gas. The thermal linewidth is given by $\Delta v(FWHM) = 2.35\sigma_v$ where $\frac{\sigma_v}{\text{km s}^{-1}} = \sqrt{\frac{T}{121 \text{ K}}}$. This could have a dramatic effect on the SPS, as discussed by LP (section 4.3), in that a given velocity width may be effectively thick for warm gas, but thin for cool gas. LP predict that changing the velocity resolution will change the SPS slope only so long as the velocity resolution is less than the thermal velocity width. The lower panel of figure 8 shows that the steepening of the SPS slope in region 2 stops at velocity width of about 6 km s^{-1} . This is rather broad for the **thermal** width of the cool phase gas, however 6 km s^{-1} matches quite well the random velocity of the cool HI clouds (Belfort and Crovisier 1984). Thus the implication of figure 8 is that at low z , where the cool phase of the HI dominates, the turbulent **velocity** field dominates the emission fluctuations, whereas at higher z , where there is little cool HI relative to warm, the **density** fluctuations dominate.

The numbers indicated for region 2 on figure 8 are significantly lower than for region 1; the power law index varies from about -2.65 to about -3.1. The much smaller increase in slope with increasing velocity width in this case suggests that we are now in the regime dominated by velocity fluctuations, rather than density fluctuations as in region 1. The narrow band slope of -2.65 is in good agreement with the Kolmogorov prediction for the velocity dominated regime (-2.67), but the steeper slope of -3.1 for the broader velocity slices does not match the Kolmogorov prediction of -3.33, based on $m = \frac{2}{3}$. Taken at face value, our slope change suggests that $m \simeq 0.2$, that is a much shallower slope than in the Kolmogorov case, implying more energy on small scales than in the classical theory. These numbers are remarkably similar to the power-law index of -2.8 found for **molecular clouds**,

using the optically thick lines of ^{12}CO and ^{13}CO as tracers (Stützki et al. 1998; Bensch et al. 2001). This points out that optically thick gas may show a significantly different SPS slope from the optically thin case. Further modifications of the LP theory are needed in order to relate the 2-D and 3-D properties of gas in the optically thick regime.

Recent measurements of the SPS of the HI in the SMC (Stanimirovic & Lazarian 2001, in preparation) suggest that in that environment the velocity fluctuations dominate the density fluctuations even for the warm medium. The SPS in the SMC shows a gradual steepening of the power-law slope, from -2.8 to -3.3 , with velocity averaging width. This is quite close to what would be expected for Kolmogorov turbulence ($m = \frac{2}{3}$), for an optically thin tracer for which velocity fluctuations dominate. Comparison with the spectra obtained for region 1 suggests that while the SMC has more power on smaller scales, the energy cascades faster in the Milky Way than in the SMC.

4. Conclusions

This is the first study of the Galactic HI spatial power spectrum to make use of the technique of large-scale mosaicing that was pioneered by Staveley-Smith et al. (1995) in their mapping of the SMC. This technique allows analysis of many interferometer primary beam areas together, at the full resolution of the maximum interferometer baseline. Combining the single dish and interferometer data gives us an effective range of spatial frequencies of more than a factor of 30. In addition, the mosaicing technique removes most of the effect of the attenuation due to the primary beam of the interferometer, that was a complication in earlier single-field interferometer studies of the HI in the Milky Way. One motivation for this analysis was to confirm the data quality of the SGPS, and particularly the relative calibration of the brightness on large and small angular scales. The smoothness of the power laws at low spatial frequencies on Figure 3 demonstrates that the SGPS images do not suffer from systematic bias between the single dish and interferometer data, or from missing baselines on the uv plane.

The results for the SPS slopes agree with the general prediction of turbulence theory that the slope should steepen when we make the transition from thin to thick slices (LP equation 28). Looking in more detail at the change of slope vs. velocity averaging in section 3.1 above, we find that the data for region 1 suggest that in the warm phase HI the SPS is dominated by **density** fluctuations, that match the Kolmogorov prediction quite well ($n = -4$ is observed, vs. the predicted $n = -\frac{11}{3}$). Apparently velocity fluctuations have little effect in this regime. However at lower latitudes in region 2 we find that velocity fluctuations dominate, with the very shallow spectral index of $m = 0.2$. This interpretation

may require further theoretical analysis taking account of the optical depth of the cool gas.

The larger significance of the change of slope with velocity width is that it provides support to the overall interpretation that the small scale structure of the ISM is governed by a turbulence cascade. This has long been the paradigm for interpretation of the structure function of the **ionized** gas, but it has only recently been extended to cover the structure of the neutral medium as well. There is some evidence that extending the SPS down to the very small angular scales sampled by VLBI observations of 21-cm absorption variations (Faison et al. 1998) shows that even this “tiny scale structure” (Heiles 1996) is consistent with the same cascade (Deshpande 2000).

As a disclaimer we must point out that the results presented here, are derived only from small areas that may not be representative of the Milky Way disk as a whole. It is very likely that different regions of the galaxy have very different characteristics that may be reflected in differences in the statistics of their small scale density and velocity fields. The differences between the two regions studied here may not nearly span the range of possibilities for the real ISM. Only a comprehensive study of the data from the entire SGPS area will show how diverse the HI spatial power spectrum may be. On the theoretical side, questions remain about how the energy of the turbulence cascades from large to small scales, whether some is lost by dissipation at intermediate scales since the medium almost certainly is compressible, and how the irregularities in the density and velocity fields are coupled. These fundamental questions are beyond the scope of this study, but we can hardly begin to understand interstellar turbulence until we can answer them.

Observationally, the results presented here for the spatial fluctuations of the 21-cm **emission** are critical for the measurement and interpretation of the 21-cm **absorption** in the SGPS. This will be the topic of a forthcoming paper.

5. Acknowledgements

We are very grateful to the ATNF staff for their assistance and encouragement at all stages of this project, and in particular to Robin Wark and John Reynolds for their support. We are grateful to Avinash Deshpande, David Green, Itzhak Goldman and the anonymous referee for suggestions and comments on the manuscript. B.M.G. acknowledges the support of NASA through Hubble Fellowship grant HST-HF-01107.01-A awarded by the Space Telescope Science Institute, which is operated by the Association of Universities for Research in Astronomy, Inc., for NASA under contract NAS 5-26555. N.M. M.-G. is supported by NASA Graduate Student Researchers Program GSRP) Fellowship NGT 5-50250. This research was

supported in part by NSF grant AST 97-32695 to the University of Minnesota.

REFERENCES

Allen, R.J. 2001, in **Gas and Galaxy Evolution** ASP Conference Series, eds. J.E. Hibbard, M.P. Rupen, and J.H. van Gorkom, (San Francisco, ASP) in press.

Belfort, P. and Crovisier, J. 1984, A&A136, 368.

Bensch, F., Stützki, J., and Heithausen, A., 2001, A&A 366, 636.

Burton, W.B., 1971, A&A 10, 76.

Burton, W.B., 1988, in **Galactic and Extragalactic Radio Astronomy**, 2nd ed., eds. G.L. Verschuur and K. Kellerman, (New York : Springer-Verlag) p. 295.

Brault, J.W. and White, O.R., 1971 A&A 13, 169.

Cordes, J.M., and Rickett, B.J. 1998 ApJ 507, 846.

Crovisier, J., and Dickey, J.M., 1983, A&A 122, 282.

Deshpande, A.A., 2000, MNRAS, 317, 199.

Deshpande, A.A., Dwarakanath, K.S., and Goss, W.M., 2000 ApJ 543, 227.

Dickey, J.M., McClure-Griffiths, N., Gaensler, B., Green, A., Haynes, R., Wieringa, M. 1999, in **New Perspectives on the Interstellar Medium**, ASP Conference Series 168, eds. A.R. Taylor, T.L. Landecker, and G. Joncas (San Francisco, ASP) p. 27.

Dickman, R.L., Margulis, M., Horvath, M.A. 1990, ApJ 365, 586.

Elmegreen, B.G., Kim, S., and Staveley-Smith, L. 2001, ApJ 548, 749.

Faison, M.D., Goss, W.M., Diamond, P.J., Taylor, G.B., 1998, AJ 116, 2916.

Fich, M., Blitz, L., and Stark, A.A., 1989, ApJ342, 272.

Gautier, T.N., Boulanger, F., Perault, M., and Puget, J.L., 1992, AJ 103, 1313.

Goldman, I. 2000 ApJ 541, 701.

Green, D.A., 1993, MNRAS 262, 327.

Heiles, C., 1997, ApJ 481, 193.

Kalberla, P.M.W., and Stenholm, L.G., 1983, Mitteil. Astron. Gesellschaft, 60, 397.

Kaplan, S.A., 1966, **Interstellar Gas Dynamics** (Oxford: Pergamon Press) p.123 ff.

Lazarian, A. and Pogosyan, D. 2000 ApJ 537, 720.

McClure-Griffiths, N.M., Dickey, J.M., Gaensler, B.M., Green, A.J., Haynes, R.F., Wieringa, M.H., 2000, AJ 119, 2828.

McClure-Griffiths, N.M., Green, A.J., Dickey, J.M., Gaensler, B.M., Haynes, R.F., Wieringa, M.H., 2001, ApJ in press.

Padoan, P., Kim, S., Goodman, A., Staveley-Smith, L., 2001, Ap. J. in press (astro-ph 11122P).

Rickett, B.J. 1977, ARA&A 15, 479.

Sault, R.J., Staveley-Smith, L., and Brouw, W.N., 1996, A&A Supplements, 120, 375.

Spangler, S.R. 2001, Space Science Reviews, in press.

Stanimirović, S., Staveley-Smith, L., Dickey, J.M., Sault, R.J., and Snowden, S.L., 1999, MNRAS 302, 417.

Stanimirović, S. 1999, Ph.D. Thesis, University of Western Sydney Nepean, p. 157.

Staveley-Smith, L., Sault, R.J., McConnell, D., Kesteven, M.J., Hatzidimitriou, D., Freeman, K.C., and Dopita, M.A., 1995, PASA 12,13.

Stützki, J., Bensch, F., Heithausen, A., Ossenkopf, V., and Zielinsky, M., 1998 A&A 336, 697.

Westpfahl, D.J., Coleman, P.H., Alexander, J., and Tongue, T. 1999 AJ 118, 323.

Zielinsky, M. and Stützki, J., 1999 A&A 347, 630.

This figure "f1.jpg" is available in "jpg" format from:

<http://arxiv.org/ps/astro-ph/0107604v1>